

REFLECTION SUPPRESSION IN CYLINDRICAL NEAR-FIELD ANTENNA MEASUREMENT SYSTEMS – CYLINDRICAL MARS

Stuart Gregson, Allen Newell, Greg Hindman
Nearfield Systems Inc.
19730 Magellan Drive,
Torrance, CA 90502-1104

ABSTRACT

Reflections in antenna test ranges can often be the largest source of measurement error within the error budget of a given facility [1]. Previously, a technique named Mathematical Absorber Reflection Suppression (MARS) has been used with considerable success in reducing range multi-path effects in spherical near-field antenna measurements [2, 3, 4, 5]. Whilst the technique presented herein is also a general purpose measurement and post-processing technique; uniquely, this technique is applicable to cylindrical near-field antenna test ranges. Here, the post-processing involves the analysis of the cylindrical mode spectrum of the measured field data which is then combined with a filtering process to suppress undesirable scattered signals.

This paper provides an introduction to the measurement technique and a description of the novel near-field to far-field transform algorithm before presenting preliminary results of actual range measurements. These results illustrate the success of the technique by showing a *circa* 10 to 20 dB reduction in spectral reflections (*i.e.* a reduction in the scattering from a known scatterer within the measurement environment) which is comparable to the degree of improvement attained with the pre-existing, comparable, spherical MARS technique.

Keywords: Near-Field, Antenna Measurements, Reflection Suppression, Cylindrical Mode Expansion, MARS.

1. Introduction

This paper describes new a technique which has been developed by NSI in order to suppress reflections in a cylindrical near-field antenna test range. Here, a unique measurement and mathematical post processing technique is implement that, as will be shown below, requires a minimum amount of detailed information about the AUT, probe and range geometry. The processing is applied during the near-field to far-field transformation process and is implemented efficiently by means of the fast Fourier transform (FFT) algorithm. The technique is entirely generic in nature and can be applied to a variety of different antenna types, *i.e.* no specific a priori assumptions about the type of AUT are made. In essence, a new mathematical operator is applied to the measured data that orthogonalises those field associated with the AUT from those fields associated with other spurious sources. In this way, the unwanted contributions can be effectively filtered out.

However, successful processing requires that a larger amount of data be taken during the measurement process than would be the case for an equivalent measurement of an identical antenna installed within an ideal anechoic environment. Thus, the price of the filtering is an increase in the time required to take a near-field measurement.

2. Overview of Measurement Technique & Transform

Typically, an antenna is installed within a near-, or far-field facility such that it is displaced in space as little as possible during the course of a measurement. As range multi-path tends to disturb the fields illuminating the test antenna, the purpose of this strategy is to insure that the field illuminating the test antenna changes as little as possible during the course of the acquisition. However, the MARS measurement technique adopts a fundamentally opposing strategy where by the test antenna is deliberately displaced from the centre of rotation. This has the effect of making the differences in the illuminating field far more pronounced than would otherwise be the case, and it is exactly this greater differentiation that makes their identification and subsequent removal viable. Figure 1 below shows an AUT installed within a typical cylindrical near-field measurement system, centred about the origin of the range co-ordinate system. Figure 1 also shows the (*z*-axis truncated) conceptual smallest cylinder that circumscribes the majority of the current sources which is coaxial with the sampling cylinder that is formed from the intersection of linear and rotational axes.

It is well known that the electromagnetic fields outside an arbitrary test antenna radiating into free space can be expanded into a set of orthogonal cylindrical mode coefficients (CMCs) and that these modes and coefficients can then be used to obtain the electric and magnetic fields everywhere in space outside of a conceptual cylindrical surface which encloses the radiator [6, 7, 8]. The CMCs are determined from the measured data in a very efficient manner through the use of the FFT. Once obtained, these mode coefficients are corrected for the spatial filtering properties of the near-field probe to determine the true AUT transmitting CMCs. A highly efficient FFT based summation process is then utilised to obtain the asymptotic far electric field. Parameters such as copolar, cross-polar, axial ratio, tilt angle, directivity and gain of the AUT are obtained from the electric field where the resulting pattern data is tabulated on a regular azimuth over elevation co-

ordinate system and resolved onto a Ludwig II, azimuth over elevation polarisation basis.

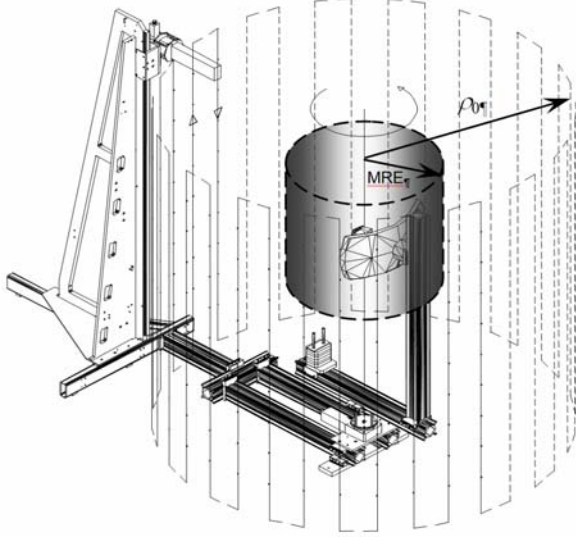


Figure 1 – Cylindrical measurement system showing conceptual cylindrical maximum radial extent.

When expressed in component form, and when assuming an infinitesimal Hertzian dipole probe is employed as a near-field probe (this assumption is merely introduced to simplify the pedagogy), the two sets of orthogonal CMCs $B_n^{(1)}(\gamma)$, $B_n^{(2)}(\gamma)$ can be obtained from,

$$B_n^{(1)}(\gamma) = \frac{-1}{4\pi^2 \kappa^3 H_n^{(1)}(\kappa \rho_0)} \int_{-\infty}^{\infty} \int_0^{2\pi} \left[\frac{n\gamma}{\rho_0} E_z(\rho_0, \phi, z) + \kappa^2 E_\phi(\rho_0, \phi, z) \right] e^{-j(n\phi + \gamma z)} d\phi dz \quad (1)$$

$$B_n^{(2)}(\gamma) = \frac{k_0}{4\pi^2 \kappa^2 H_n^{(1)}(\kappa \rho_0)} \int_{-\infty}^{\infty} \int_0^{2\pi} [E_z(\rho_0, \phi, z)] e^{-j(n\phi + \gamma z)} d\phi dz \quad (2)$$

Here, the Fourier variable γ can take on all real values from negative to positive infinity and the modal index can take on all real values from negative to positive infinity. Here, ϕ and z are used to denote the azimuthal and linear cylindrical co-ordinates respectively with γ and z being conjugate variables. ρ_0 is the radius of the measurement cylinder, k_0 is the free-space wave number, $H_n^{(1)}(z)$ is the Hankel function of the first kind, $H_n^{(1)\prime}(z)$ is the derivative of the Hankel function of the first kind, and j is the imaginary unit. Crucially, both (1) and (2) are in a form that is instantly amenable for processing with the efficient two-dimensional FFT algorithm although this results in the use of non-integer mode indices. Once the transverse electric (TE) and transverse magnetic (TM) CMCs have been determined, by utilising the large argument values of the Hankel function and the derivative of the Hankel function,

$$H_n^{(1)}(\kappa \rho_0) \approx (-j)^n \sqrt{\frac{2}{\pi \kappa \rho_0}} e^{j(\kappa \rho_0 - \pi/4)} \quad (3)$$

$$H_n^{(1)\prime}(\kappa \rho_0) \approx j H_n^{(1)}(\kappa \rho_0) \quad (4)$$

Thus, the asymptotic far-field pattern can be obtained from a simple summation of mode coefficients as follows,

$$E_\theta(r \rightarrow \infty, \theta, \phi) = 2jk_0 \sin \theta \sum_{n=-\infty}^{\infty} (-j)^n B_n^{(2)}(\gamma) e^{jn\phi} \quad (5)$$

$$E_\phi(r \rightarrow \infty, \theta, \phi) = -2k_0 \sin \theta \sum_{n=-\infty}^{\infty} (-j)^n B_n^{(1)}(\gamma) e^{jn\phi} \quad (6)$$

$$E_r(r \rightarrow \infty, \theta, \phi) = 0 \quad (7)$$

$$\underline{H}(r \rightarrow \infty, \theta, \phi) = \frac{\hat{e}_r \times \underline{E}(r \rightarrow \infty, \theta, \phi)}{Z_0} \quad (8)$$

Here, and as per the usual convention, the unimportant far-field spherical phase factor and inverse r term have been suppressed. Similarly, (5) and (6) are in form that can be evaluated with the use of a one-dimensional inverse FFT. The maximum mode index N is given by,

$$N = k_0 r_t + 10 \quad (9)$$

Where r_t is the maximum radial extent (MRE) which includes a ‘‘safety’’ margin of 10 [9]. Unfortunately, in practice for some antennas the size of the MRE may not be obvious. As only propagating modes can contribute to the far-field pattern, the Fourier variable γ can be limited to $\pm k_0$ as these represent the highest order propagating mode coefficients. This also places a limit on the sample spacing required to obtain alias free data. As the sample spacing δ_z (*i.e.* the resolution) in the linear axis is determined from the maximum value of γ , we can write that $\delta_z = \lambda/2$ where λ is used to denote the free-space wavelength. Similarly, the sample spacing in the angular dimension is obtained from the highest order mode index [9],

$$\delta\phi = 2\pi/(2N + 1) \quad (10)$$

Clearly then, by displacing the AUT away from the centre of rotation, the MRE is increased. This decreases the sample spacing which increases the amount of data needed and therefore time required to acquire the complete near-field data set. The last remaining parameter that needs to be determined is the range length, *i.e.* the radius of the conceptual measurement cylinder. This is specified as being the larger of the two following requirements [9],

$$\rho_0 \geq \begin{cases} r_t + r_p + 10/k_0 \\ r_t + 3\lambda \end{cases} \quad (11)$$

Where, r_p is the maximum radial extent of the probe. This quantity would have been determined during the probe’s auxiliary pattern calibration. Once the probe corrected electric far-fields have been determined, the phase reference can be displaced by means of the application of a simple differential phase change [10], *i.e.*,

$$\underline{E}_r(r \rightarrow \infty, \theta, \phi) = \underline{E}(r \rightarrow \infty, \theta, \phi) e^{j\hat{k}_0 \cdot \underline{r}} \quad (12)$$

Here, \underline{r} denotes the displacement vector between the centre of the measurement co-ordinate system and the centre of the aperture of the AUT. Crucially, whilst in principle all we have done is to mathematically translate the AUT back to the centre of the measurement co-ordinate system, this has the corresponding effect of reducing the number of

CMCs that are required to represent the radiated field. That is, we have reduced the MRE to a conceptual (*i.e.* optimised) minimum value. The equivalent cylindrical mode coefficients that represent the displaced antenna can be obtained from an inversion of equations (5) and (6) which again can be evaluated numerically through the use of the one-dimensional inverse FFT. Thus,

$$B_n^1(\gamma) = -\frac{(-j)^{-n}}{4\pi\kappa} \int_0^{2\pi} E_\phi(r \rightarrow \infty, \theta, \phi) e^{-jn\phi} d\phi \quad (13)$$

$$B_n^2(\gamma) = -j \frac{(-j)^{-n}}{4\pi\kappa} \int_0^{2\pi} E_\theta(r \rightarrow \infty, \theta, \phi) e^{-jn\phi} d\phi \quad (14)$$

The factor of 2π is introduced on the denominator in (13) and (14) to preserve the correct normalisation of the CMCs. Once the cylindrical mode coefficients for the, now ideally centrally located, AUT have been recovered, any mode representing fields outside the ideal MRE can be filtered out thus removing contributions that are not associated with the AUT. This is determined using [8],

$$n^2 + (\gamma r_{i0})^2 > (k_0 r_{i0})^2 \quad (15)$$

Here, r_{i0} denotes the optimum MRE, rather than the actual MRE as taken from the near-field measurement where $r_i > r_{i0}$. The mode cut-off is based on the fact that modes above a certain index number are exponentially attenuated and do not contribute to the far-field. Thus in effect, the mode cut off is determined by the physical dimensions of the AUT. The final step in the processing is to reconstruct the filtered far-field antenna pattern from equations (5) and (6). The cylindrical MARS algorithm can be summarised as follows:

1. Take the two orthogonal tangential electric cylindrical near-field components (E_ϕ , E_z) and perform a 2-D FFT on each component.
2. Compute $B_n^1(\gamma)$ and $B_n^2(\gamma)$ from the results of the 2-D FFT of each measured field component.
3. Solve for the Antenna's unknown cylindrical mode coefficients using previously computed probe pattern coefficients.
4. Perform a 1-D FFT to obtain the far-field azimuth antenna pattern for a particular elevation angle. Compute the complete far-field pattern by repeating this for each discrete elevation angle.
5. Apply a differential phase change to mathematically translate the AUT back to the origin of the measurement co-ordinate system.
6. Perform a 1-D IFFT to obtain the translated CMC of the AUT for a particular γ . Repeat this for each discrete value γ .
7. Apply two-dimensional mode filtering function to suppress unwanted CMCs.
8. Perform a 1-D FFTs to obtain far-field azimuth antenna pattern for a particular elevation angle. Compute the complete far-field pattern by repeating this for each discrete elevation angle to obtain the MARS filtered AUT pattern function.

Whilst a certain degree of effort is required to calculate the CMCs from the far-field pattern, and then reconstruct the far-field pattern from the filtered set of CMCs, as neither of these operations requires us to compute a Hankel function (or their derivative), and since the transforms are evaluated with the FFT, these operations are actually very cost effective in terms of computational effort, especially when compared to other alternative strategies.

3. Preliminary Measured Results

In order that the new measurement and post-processing technique could be verified, an NSI-200V-3x3 combination planar/cylindrical/spherical system was used to test a 12" wide by 11.6" high x-band slotted waveguide planar array antenna.

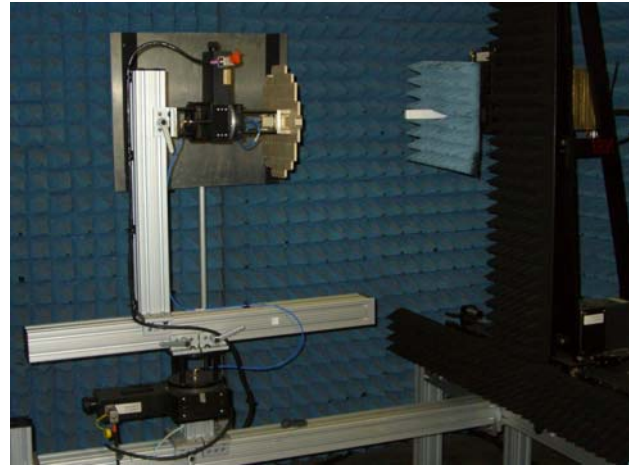


Figure 2 – NSI-200V-3x3 PCS System measuring slotted array antenna in the presence of a reflecting plate.

This system was installed in one of NSI's small, partially lined anechoic chambers and included, and employed an Agilent 85301b RF subsystem. A small removable reflecting plate was installed within the chamber to maximise the scattering and create a "worst case" configuration. This arrangement can be seen presented in Figure 2 where it is also worth noticing that much of the scanner's structure is not covered with absorber which further exacerbates the scattering.

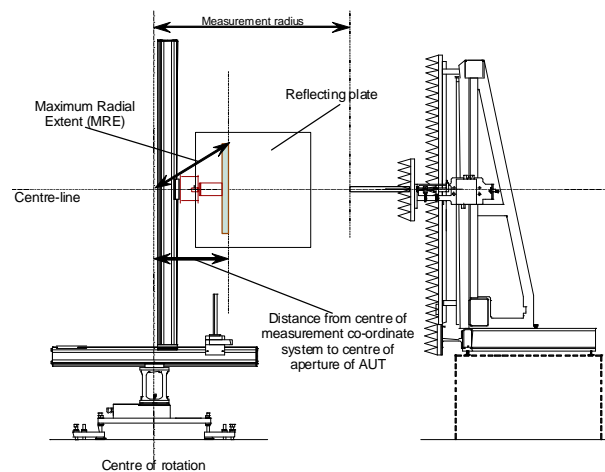


Figure 3 – Schematic of NSI-200V-3x3 PCS System.

When taking a standard cylindrical near-field measurement, certain parameters are required to be specified. These are the frequency, 9.2 GHz, the radius of the measurement cylinder, 24.625", the MRE, 16", the required far-field azimuth, 360°, and elevation, ~20° spans. In addition to this, a pattern for the near-field probe is also required. As an NSI-RF-WR90 open-ended rectangular waveguide probe was used, a theoretical probe pattern was employed to correct the measured data [11]. In addition to this, for the purposes of cylindrical MARS testing, the displacement between the centre of the range measurement co-ordinate system and the AUT, and the conceptual minimised MRE are also needed. These were 15" and 6.3" respectively. This arrangement can be seen presented schematically in Figure 3.

CMCs are complex numbers that are functions of the polarization index, the ϕ index n and the Fourier variable γ . Figure 4 contains a plot of the amplitudes of the CMCs modes for $s = 1$, *i.e.* B^1 , for this measurement which were generated by the regular cylindrical processing of the measured cylindrical near-field data.

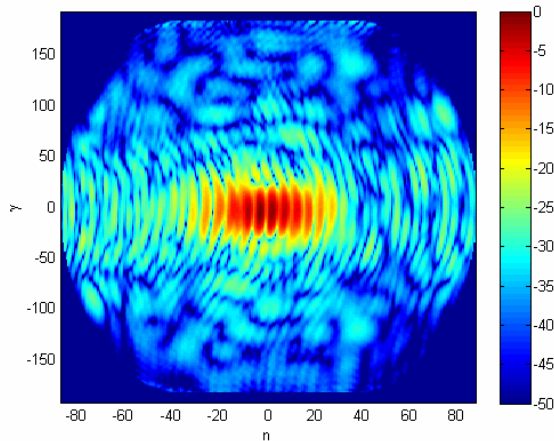


Figure 4 – B^1 CMCs derived directly from measured near-field data.

The offset in the near-field measurement causes the phase of the scattered signals to vary rapidly over the measurement cylinder and to produce the higher order modes shown. Clearly, the CMCs obtained from the near-field measured data shown in Figure 4 contain contributions from both the AUT and the scatterer. In the domain of the CMCs, these two sources are interfering constructively and destructively as a function of mode index. After applying the differential phase change to the equivalent far-field pattern to mathematically displace the AUT so that its phase centre (*i.e.* aperture) is coincident and synonymous with the origin of the cylindrical measurement co-ordinate system, the contributions in the domain of the CMCs are separated, *i.e.* displaced so that they no-longer interfere with one another. This is shown in Figure 5. Here, modes associated with the AUT are tightly distributed about the $n = 0$, *i.e.* in the centre of the plot, whilst the modes associated with the scatterer can be seen to be distributed about the $n = -75$ mode index. Thus, the

two sources have been separated, *i.e.* orthogonalized in the CMC domain.

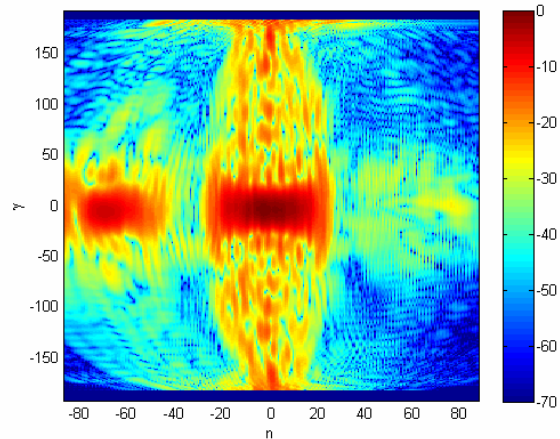


Figure 5 – B^1 CMCs once the AUT has been conceptually translated to the origin of the measurement co-ordinate system.

Furthermore, as the mode coefficients associated with the AUT are within the $k_0 r_0$ region of mode space, any coefficients outside of this region of the domain can be removed without prejudice to the far-field antenna pattern function. Although the filtering is normally based on the aperture size of the antenna this may be increased for analysis purposes up to a limit determined by the near-field data point spacing as shown here. Figure 6 below contains a plot of the CMCs after filtering.

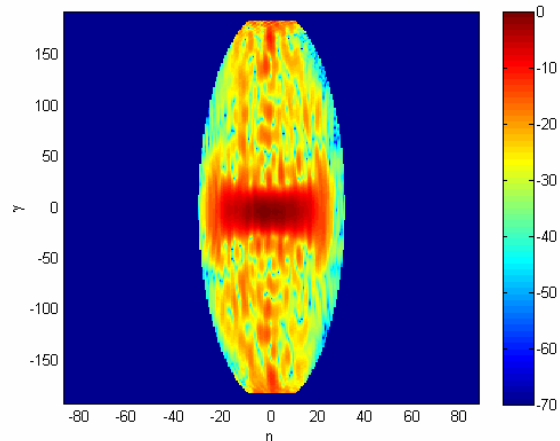


Figure 6 – B^1 CMCs shown after MARS filtering.

In this case, the minimum cylinder which contains the translated antenna aperture causes the cylindrical MARS processing to filter out all higher order modes above $|N| = 31$ as these modes can not be part of the antenna's far-field radiation pattern. Although not shown herein, similar plots can be created for the linearly independent set of B_2 CMCs. Figure 7 contains a plot of the probe corrected far-field pattern of the AUT that is obtained from the cylindrical near-field data prior to cylindrical MARS filtering. Here, it is clear that with the reflecting panel, the measurements contain significant range multi-path with a large response being visible at $Az = 80^\circ$, $El = 0^\circ$ originating from the spectral reflection from the panel. The reflections at -150°

to -70 deg in Az are most likely a result of the scattering off the side of the RF equipment rack that is situated immediately outside the small chamber as no door is fitted.

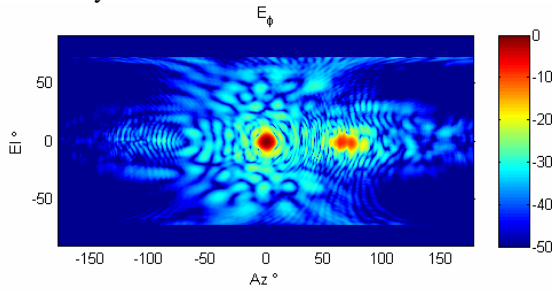


Figure 7 – Far-field pattern of x-band slotted waveguide array antenna.

Figure 8 contains an equivalent plot that was obtained using the same cylindrical near-field data set as was used above only this time; the cylindrical MARS process was employed to filter out artefacts arising from range multipath.

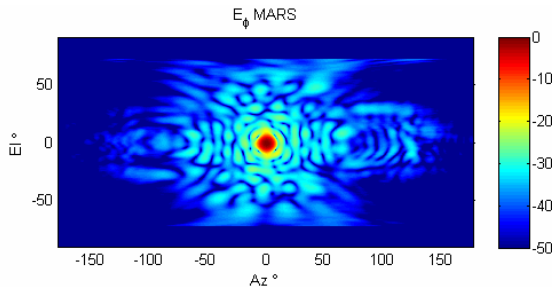


Figure 8 – Far-field pattern of x-band slotted waveguide array after MARS processing.

From inspection, it is quite evident that the main specular reflection that was evident at $Az = 80^\circ, Ei = 0^\circ$ has been almost completely suppressed. Furthermore, the high frequency angular ripple that was evident in the unfiltered results is clearly absent in this result, which is very encouraging. Due to the large measurement radius and the comparatively short travel of the linear scan axis, $3'$, these patterns suffer a significant amount of truncation the elevation plane and the pattern data at larger angles is rendered unreliable as a result of the onset of the first order truncation effect [10].

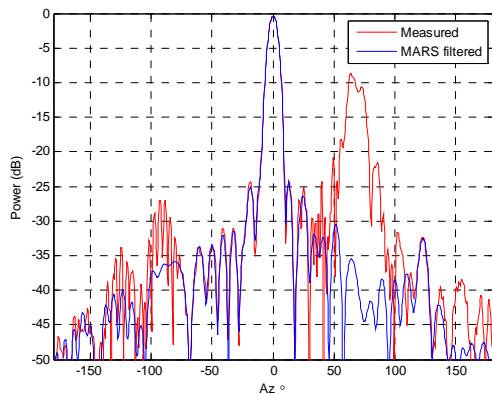


Figure 9 – Far-field pattern of x-band slotted waveguide array shown before, and after MARS processing.

From inspection of Figure 9, it is very evident that the comparison of the azimuth cuts with, and without MARS filtering it can be seen that the spurious reflection at 80° has been suppressed by *more* than 25 dB. Again, it is clear that the overall spurious high frequency ripple that is evident on the red trace can be seen to have been suppressed on the blue, MARS filtered trace. By way of a further illustration Figure 10 contains a comparison plot of AUT measured without the reflecting plate, which is used as a reference “truth model”, and the MARS filtered measurement with the reflecting plate. Here, red contours (*i.e.* isolevels) are used to denote the cylindrical MARS filtered antenna pattern without the reflecting plate whilst the black contours denote the cylindrical MARS filtered antenna pattern with the reflecting plate. The respective sets of contours have been plotted at $-40, -30, -20, -10, -5, -3, -2, -1$ dB levels. Again the degree of agreement is very encouraging with differences becoming visible at large elevation angles where the pattern data is outside the range of validity and for regions of lower field intensities.

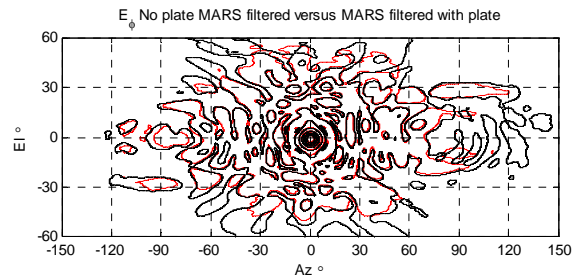


Figure 10 – Comparison of MARS filtered without plate and MARS filtered with plate results.

We can obtain a more concise graphical display by selecting the $\gamma = 0$ CMCs which correspond to the maximum amplitude and plot a graph of the mode amplitude versus the mode number n . Table 1 below shows a mode plot for the reference truth model data, *c.f.* Figure 5 for $\gamma = 0$.

Δz	CMCs @ $\gamma=0$	Far-field Azimuth Cut
$8''$		

Table 1 –Cylindrical MARS Results without reflecting plate

Here, the groupings of CMCs that are associated with the reflecting plate are absent and the equivalent far-field azimuth plot is also free of the large specular response that is clearly present within the unfiltered pattern data. Table 2 below contains similar data from a series of measurements that were taken with the reflecting plate installed within the chamber. During each of these measurements, the only parametric change that was introduced was in the displacement between the origin of the measurement co-

ordinate system and the phase centre of the AUT. The purpose of this was to try and establish a relationship between this displacement and the location of the scattering CMCs.

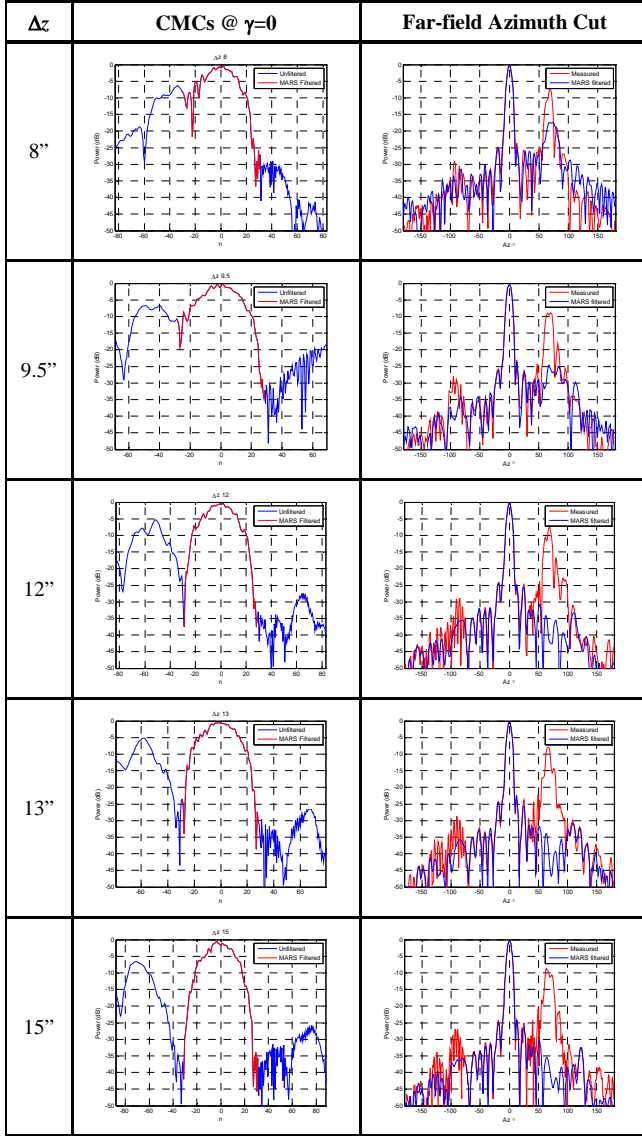


Table 2 – Summary of Cylindrical MARS Displacement Results with reflecting plate

From inspection of the figures contained within Table 2, it can be seen empirically that the centre of the distribution of CMCs that are associated with the scatterer (plotted in blue and visible to the left hand side of the mode plots) are approximately located at,

$$n = k_0 \Delta z \quad (16)$$

Here, Δz denotes the offset between the centre of rotation and the AUT. Strictly, the modes are located at negative mode indices but this is only an artefact of the location of the reflecting plate within the chamber. If the scatterer were to have been located on the opposite side of the chamber, then the distribution would correspond to positive mode indices. Crucially, irrespective of where the scattered modes are, the effect of the MARS process is to moves that

are associated with scattering object to larger magnitude mode indices, *i.e.* their distributions move away from $n = 0$. By way of confirmation, using Equation 14 for the measurements presented within Table 2, and rounding towards the nearest largest integer, yields the following results: ($\Delta z = 8.0''$, $n = 40$), ($\Delta z = 9.5''$, $n = 47$), ($\Delta z = 12.0''$, $n = 59$), ($\Delta z = 13.0''$, $n = 64$), ($\Delta z = 15.0''$, $n = 74$). All of these results are in agreement with experiment. Thus, we would want to insure that Δz is sufficiently large so that lowest order modes associated with the scatterer are outside the mode spectrum occupied by the AUT. When $\gamma = 0$, once translated back to the origin of the measurement system, the AUT occupies the mode spectrum,

$$-k_0 r_{t0} \leq n \leq k_0 r_{t0} \quad (17)$$

Where r_{t0} is the maximum radial extent (this is the conceptual maximum radial extent when the AUT is optimally installed in the range with its phase reference coincident and synonymous with the origin of the measurement co-ordinate system). Hence we need to insure that the following condition is satisfied,

$$k_0 \Delta z \gg k_0 r_{t0} \quad (18)$$

Specifically, as the quantity $k_0 \Delta z$ merely locates the nominal centre of the distribution, to insure that the outlying modes are also separated from the AUT, it is reasonable to adopt the following measurement criteria,

$$k_0 \Delta z > 2k_0 r_{t0} \quad (19)$$

Or simply that,

$$\Delta z > 2r_{t0} \quad (20)$$

Stated simply, the displacement must be larger than the diameter of the conceptual optimum MRE. In our case, this corresponds ensuring the displacement is at least a large as the diameter of the AUT and preferably larger. One way of viewing this it to suppose that the scattered mode spectra have the same range of modes as the AUT which is not unreasonable as (in the absence of any other independent sources) the scatterer is in essence merely a reflection of the AUT and we are able to determine a rule of thumb for the size of the displacement.

5. Summary, Conclusions, and Future Work

Cylindrical MARS processing can be used with a good degree of confidence since all the steps in the measurement and analysis are consistent with the well established principles of the cylindrical near-field theory and measurement techniques, and all comparisons have proved overwhelmingly positive. The offset of the AUT and the resulting smaller data point spacing are valid if the spacing satisfies the sampling criteria. The translation of the far-field pattern to the origin with the phase shift is rigorous. The selection of the mode cut-off for the translated pattern is based on the physical dimensions of the AUT and its translated location. The recommended mode cut-off is calculated from the AUT dimensions but can be modified by the user if the spherical mode plots, *e.g.* Figure 5, suggest a different cut-off is required. The results of the cylindrical MARS processing will always reduce, but not entirely eliminate, the effective of scattering. The final

result with cylindrical MARS can be degraded if the sampling of the near-field data is too large, or the mode filter is too small, but this is also true for regular cylindrical processing. Importantly, both of these parameters are controlled by the user and must be correctly specified.

NSI has developed and validated a novel technique to suppress reflections in cylindrical near-field ranges. The technique is quite general and can be used to achieve acceptable results with use of minimal absorber or even with no anechoic chamber. It can also improve the reflection levels in a traditional anechoic chamber by 10 dB or more, allowing improved accuracy as well as the ability to use existing chambers down to lower frequencies than the absorber used might indicate.

NSI has now developed reflection suppression techniques that are highly effective at improving measurements taken in spherical and now cylindrical near-field ranges. Work is ongoing to develop similar techniques for use with planar facilities.

REFERENCES

- [1] A.C. Newell, "Error Analysis Techniques for Planar Near-field Measurements", IEEE Transactions on Antennas and Propagation, vol. AP-36, pp. 754-768, June 1988.
- [2] G.E. Hindman, A.C. Newell, "Spherical Near-Field Self-Comparison Measurements", AMTA 26th Annual Meeting & Symposium, Atlanta, GA, October 2004.
- [3] G.E. Hindman, A.C. Newell, "Reflection Suppression in a large spherical near-field range", AMTA 27th Annual Meeting & Symposium, Newport, RI, October 2005.
- [4] G.E. Hindman, A.C. Newell, "Reflection Suppression To Improve Anechoic Chamber Performance", AMTA Europe 2006, Munch, Germany, March 2006.
- [5] G.E. Hindman, A.C. Newell, "Mission To MARS – In Search of Antenna Pattern Craters", AMTA 28th Annual Meeting & Symposium, St. Louis, MO, November 2007.
- [6] J. Brown and E.V. Jull, "The Prediction of Aerial Radiation Patterns From Near-Field Measurements," Proc. of the Institute of Electrical Engineers, Vol 108-B, Nov. 1961, pp. 635-644.
- [7] W.M. Leach, D.T. Paris, "Probe Compensated Near-Field Measurements On A Cylinder", IEEE Trans. on Antennas and Propagation, AP-21, No. 4, July 1973, pp. 435-444.
- [8] A.D. Yaghjian, "Near-Field Antenna Measurements On a Cylindrical Surface: A Source Scattering Matrix Formulation", NBS Technical Note 696, 1977.
- [9] J.E. Hansen (ed.), "Spherical Near-Field Antenna Measurements", The Institution of Engineering and Technology, UK, Peter Peregrinus Ltd., 1988.
- [10] S.F. Gregson, J. McCormick, C.G. Parini, "Principles of Planar Near-Field Antenna Measurements", The Institution of Engineering and Technology, UK, 2007.
- [11] A.D. Yaghjian, "Approximate Formulas for the Far Fields and Gain of Open-Ended Rectangular Waveguide", Electromagnetic Fields Division, NBSIR 83-1689, May 1983.

ACKNOWLEDGEMENTS

The authors wish to express their gratitude to Ms L. Duron and Mr S. Brown for their help with the experimental portion of this work.